RSC Advances

PAPER

View Article Online
View Journal | View Issue



Cite this: *RSC Adv.*, 2024, **14**, 39995

# $MnFe_2O_4$-loaded bamboo pulp carbon-based aerogel composite: synthesis, characterization and adsorption behavior study for heavy metals removal†

Wenxiang Jing,[abc] Chai Yang,[b] Xiaoyan Lin, *[ac] Min Tang,[b] Dongming Lian,[b] Ying Yu[b] and Dongyang Liu[b]

Heavy metal wastewater is a direct threat to the ecological environment and human health because it is highly toxic at low concentrations. Therefore, it is very important to explore and develop efficient wastewater treatment agents. $MnFe_2O_4$-loaded bamboo pulp carbon-based aerogel (MCA) is prepared by directional freeze-drying and carbonization. SEM, TEM, XPS, XRD, BET and FTIR are used to evaluate the physical and chemical properties of MCA. Meanwhile, the adsorption performances of MCA on $Pb^{2+}$, $Cu^{2+}$ and $Cd^{2+}$ are also studied by adsorption kinetics, isothermal curves and thermodynamics. The results show that the adsorption process involves chemical adsorption and physical adsorption, and the adsorption process is a spontaneous endothermic process. The maximum adsorption capacities of MCA for $Pb^{2+}$, $Cu^{2+}$ and $Cd^{2+}$ obtained in the adsorption isotherm experiments were 74.38, 84.21 and 73.63 mg $g^{-1}$, respectively, showing excellent adsorption performance for $Pb^{2+}$, $Cu^{2+}$ and $Cd^{2+}$. Therefore, the MCA has potential application for wastewater purification of heavy metals containing $Pb^{2+}$, $Cu^{2+}$ and $Cd^{2+}$, meanwhile, this study provides some guidance for the design and application of microspheres for the separation and removal of $Pb^{2+}$, $Cu^{2+}$ and $Cd^{2+}$.

Received 3rd September 2024
Accepted 15th December 2024

DOI: 10.1039/d4ra06363e

rsc.li/rsc-advances



## 1 Introduction

Water is the foundation of life, and pollution of water resources will be a disaster in the biological world. Wastewater, especially industrial wastewater, contains a large amount of toxic heavy metal ions. If not treated, it will directly threaten the safety of human, animal and plant life.[1] Heavy metals can cause protein denaturation in animals and plants, and cause damage to animal organs, life systems, and even life.[2] Many scholars have proposed various solutions, such as the precipitation method,[3,4] electrochemical method,[5] biological method,[6–8] adsorption method,[9,10] *etc.*, to treat the heavy metal contaminated wastewater. The adsorption method is currently one of the most favored methods to remove heavy metals due to the large number of adsorbents, high efficiency, simple operation, good reversibility, low cost, and strong adsorbent regeneration ability.[11]

$MnFe_2O_4$ is a promising spinel ferrite in metal oxides, and combines the advantages of iron-based and manganese-based materials.[12] In particular, the surface area of $MnFe_2O_4$ is larger than that of other spinel ferrites. Therefore, owing to its saturation magnetization, stability, and high surface area, $MnFe_2O_4$ stands out as one of the most suitable spinel ferrites for adsorbing metal ions.[13,14] $MnFe_2O_4$ typically exhibits a mixed spinel structure.[15,16] In aqueous solutions, the metal oxide particles can be hydrated and form hydroxyl groups on the surface of materials. The hydroxyl groups on the surface tend to dissociate or protonate, depending mainly on the pH in the solution. When the pH of the solution is higher than the pH of the zero charge point (PZC), the surface of the particle is negatively charged. The positive/negative charge of surface can prevent the aggregation of particles through electrostatic repulsion.[17] Therefore, $MnFe_2O_4$ has excellent redox properties for ($Fe^{2+}$/$Fe^{3+}$), conductive solid structures, and the presence of hydroxyl (–OH) reaction sites on the material surface, making it highly promising for the removal of organic and heavy metal pollutants from wastewater.[18] The primary preparation methods for $MnFe_2O_4$ including pyrolysis methods, coprecipitation methods,[19,20] microemulsion methods,[21] sol–gel methods,[22,23] and hydrothermal (solvothermal) techniques.[24,25] Among these methods, the pyrolysis method has the advantages of simple process, economic efficiency, high productivity, and high

[a]*School of Materials and Chemistry, Southwest University of Science and Technology, 621010, Mianyang, Sichuan, China. E-mail: lxy20100205@163.com*
[b]*Yibin Forestry and Bamboo Industry Research Institute, Yibin 644005, China*
[c]*Engineering Research Center of Biomass Materials, Ministry of Education, Southwest University of Science and Technology, Mianyang 621010, China*

† Electronic supplementary information (ESI) available. See DOI: https://doi.org/10.1039/d4ra06363e

selectivity. Moreover, the reaction occurs in the absence of solvents, avoiding solvent related pollution.[26]

However, $MnFe_2O_4$ has a tendency to aggregate in the liquid phase, resulting in a decrease in its surface area and lower adsorption capacity. Therefore, the modification of $MnFe_2O_4$ is very important for its application as adsorption materials. Li *et al.*[27] reported that cross-linked chitosan and polyethylene glycol (PEG) bead-supported $MnFe_2O_4$ nanoparticles were formed to adsorb $As^{3+}$, $Cd^{2+}$, $Cu^{2+}$ and $Pb^{2+}$, and the adsorption capacities were 9.90, 9.73, 43.94 and 11.98 mg $g^{-1}$, respectively. Li *et al.*[28] reported that MFBC prepared by biochar loaded with $MnFe_2O_4$ from apple branches was used for $U^{6+}$ removal, and the maximum adsorption capacity was 83.00 mg $g^{-1}$ at pH = 6.0 and 313 K. Verma *et al.*[29] reported that graphene oxide supported $MnFe_2O_4$ nanocomposite adsorbent was prepared by one pot hydrothermal method, which effectively reduced the aggregation of $MnFe_2O_4$. The adsorption process followed the pseudo second order kinetic model and Langmuir adsorption isotherm model, and the maximum adsorption capacity of $Pb^{2+}$ was 621.11 mg $g^{-1}$. Asadi *et al.*[30] reported that a $MnFe_2O_4$ spinel ferrites nanoparticles were synthesized *via* a practical co-precipitation route to investigate the zinc removal from aqueous solution. These nanoparticles could remove Zn(II) by following the Langmuir isotherm model at optimum pH = 6, with the high adsorption capacities of 454.5 mg $g^{-1}$. Güzel *et al.*[31] reported that a magnetically separable biochar composite (MWPC) was synthesized by a simple chemical coprecipitation method, using wild plant-derived biochar (WPC) and manganese ferrite nanoparticles ($MnFe_2O_4$). The maximum adsorption capacity of Pb(II) determined from Langmuir isotherms at temperatures of 293, 303, 313 and 323 K was 90.09, 97.08, 123.45 and 129.87 mg $g^{-1}$, respectively. Liu *et al.*[32] reported that $MnFe_2O_4$–biochar composite (MFBC) was successfully fabricated *via* coprecipitation method as a novel and efficient adsorbent for treating Tl(I)-contaminated wastewater. MFBC exhibited high performance across a wide pH range of 4–11, with the superior Tl(I) removal capacity (170.55 mg $g^{-1}$) based on Langmuir model (pH 6.0, a dosage of 1 g $L^{-1}$).

Bamboo pulp, as a natural raw material, plays an important role in the fields of papermaking and artificial fibers.[33] Its cellulose content is very high, reaching 90–98%.[34,35] However, compared to wood pulp, it has only one narrow application field. Bamboo cellulose is a high molecular weight polymer composed of many glucose units connected by β-1,4-glycosidic bonds, with linear, rigid, and highly oriented structural characteristics.[37–39] Therefore, the internal hydrogen bonding leads to high crystallinity, small internal gaps, and single physical and chemical properties. The main active group is only hydroxyl, which greatly limits the adsorption capacity and efficiency. As cellulose has appreciable carbon content, is readily available, renewable and has a proven ability for sorption, it can be a suitable material for the preparation of carbonaceous adsorbent.[36] Nevertheless, the performance characteristics of bamboo pulp carbon aerogel based adsorbent materials mainly depend on factors such as their structural morphology, specific surface area, pore structure, and functional group type. Therefore, by adjusting key factors such as pore size and pore orientation, the solvent transport capacity can be enhanced and the transport efficiency can be improved.[40] However, the preparation process of adsorbent materials with controllable compositions remains difficult. And expensive precursors, surfactants, and organic solvents need to be added in previous complex synthesis procedures. Therefore, it is highly desirable to develop cost-effective and environmentally friendly raw materials and methods to synthesize adsorbent materials for large-scale applications in water treatment.

Developing simple, green and efficient synthetic methods has always been the goal of many scientists. Therefore, in this paper, the green and renewable bamboo pulp was mainly used as the substrate, and $MnFe_2O_4$ was introduced into the bamboo pulp hydrogel by *in situ* loading, and the $MnFe_2O_4$-loaded bamboo pulp carbon-based aerogel (MCA) was obtained by simple freeze-drying and carbonization. By these steps $MnFe_2O_4$ was uniformly distributed on the carbon aerogel. The size of $MnFe_2O_4$ particles was adjusted by studying the amount of raw materials, reaction temperature, reaction time and other factors, and the effect of $MnFe_2O_4$ particle size on the adsorption of $Pb^{2+}$, $Cu^{2+}$, $Cd^{2+}$ and other ions was also studied. By analyzing the surface morphology, element composition, particle size, crystal structure, pore size, adsorption selectivity coefficient and adsorption capacity of MCA, the structure–activity relationship of MCA for selective adsorption of heavy metals was established. The structural design, adsorption kinetics, adsorption isothermal curve and thermodynamic parameters were studied to reveal the carbonization of bamboo pulp and the structural regulation and adsorption mechanism of bamboo pulp carbon based aerogel adsorption material. The adsorption mechanism of $Pb^{2+}$, $Cu^{2+}$ and $Cd^{2+}$ was revealed by studying the adsorption kinetics, adsorption isotherm and thermodynamic parameters.

## 2 Material and methods

### 2.1 Chemicals and materials

Bamboo pulp was obtained from Sichuan Tianzhu Bamboo Resources Development Co., Ltd, Yibin, China. *N*-Methyl morpholine-*N*-oxide, (NMMO) (AR, purity ≥ 99%) was purchased from Bide Pharmatech Ltd, Shanghai, China. $Fe(NO_3)_3 \cdot 9H_2O$ (AR, purity ≥ 99%), $Mn(NO_3)_2 \cdot 6H_2O$ (AR, purity ≥ 98%), $Pb(NO_3)_2$ (AR, purity ≥ 99%), $Cu(NO_3)_2$ (AR, purity ≥ 99%) and $Cd(NO_3)_2$ (AR, purity ≥ 99%) were purchased from West Asia Chemical Technology (Shandong) Co., Ltd, Linyi, China. The experimental water was self-made, resistivity ≥ 18.25 MΩ cm.

### 2.2 Preparation of MCA

Firstly, a series of mixed solutions were prepared. 4 additives in different proportions ($Mn(NO_3)_2$ and $Fe(NO_3)_3$ powder) were weighed, with weights of 0 g and 0 g, 0.3132 g and 0.7065 g, 0.6264 g and 1.4132 g, 0.9395 g and 2.1197 g, respectively, and diluted to 100 mL volumetric flasks.[41] Then, 3.04 mL of the above solutions and 20 g of NMMO powders were transferred to four 50 mL beakers in turn. After the mixtures were completely

scattered at 90 °C, 0.31 g of bamboo pulps were added in turn, and the mixtures were stirred and heated for 120 min, pour into the mold to cool down, the formed gels were aged overnight at room temperature, and then soaked with water to replace the NMMO in the gel to prepare hydrogels with different added amounts (among the four hydrogels obtained, the mass fraction of $Mn(NO_3)_2$ and $Fe(NO_3)_3$ in the mass of bamboo pulp were 0%, 10%, 20% and 30%). Then, the pure water in the hydrogel was replaced by repeated immersion in 20% *tert*-butanol–water solution, pre-frozen in liquid nitrogen at −196 °C, and freeze-dried for 48 h. Finally, the prepared aerogel was put into a tube furnace, and then nitrogen gas was passed through to replace the air in the tube. The temperature was heated to 500 °C and carbonized for 5 h at 5 °C $min^{-1}$ and $N_2$ flow rate of 100 mL $min^{-1}$. Then it was naturally cooled to room temperature, and the sample MCA was obtained in turn and put into the dryer for later use. Samples MCA1-1, MCA1-2, MCA-1–3, and MCA1-4 represented the additives of 0%, 10%, 20% and 30%, respectively.

The mixture of 0.6264 g $Mn(NO_3)_2$ and 1.4132 g $Fe(NO_3)_3$ additives were accurately weighed and synthesized according to the above method. MCA2-1, MCA2-2 and MCA2-3 were obtained by carbonization at 300, 600 and 700 °C, respectively.

### 2.3 Characterization

The morphology analysis of the samples was tested by SEM (Regulus 8100, Hitachi, Japan) and TEM (Tecnai G2 F20, FEI, USA). The specific surface area/porosity of the samples were analyzed by a BET surface area measurement (ASAP 2020, Micromeritics, USA). The DFT model was used to analyze the porosity. The surface functional groups and composition were analyzed by XPS (Escalab 250Xi, Thermo Fisher, USA), and the surface functional groups of the samples were measured by FTIR (IRAffinity-1S, Shimadzu, Japan) using the potassium bromide table-pressing technique, which was detected in the wavelength range of 400 to 4000 $cm^{-1}$. The composition information of the samples was obtained by XRD (Bruker AXS, Germany). The X-ray source was Cu-K$\alpha$. The tube voltage was 40 kV, the tube current was 40 mA, and the scanning range was $2\theta$ = 10–80°. The charge properties of the sample surface were measured by a zeta potential analyzer (Zetasizer Nano ZS).

### 2.4 Adsorption experiment of $Pb^{2+}$, $Cu^{2+}$ and $Cd^{2+}$

The adsorption performance of MCA were evaluated using single or multi-component heavy metal solutions ($Pb^{2+}$, $Cu^{2+}$ and $Cd^{2+}$). The solution was adjusted to the desired pH by 0.1 mol per L sodium hydroxide or hydrochloric acid. 0.03 g of MCA was put into a 150 mL conical flask, and 50 mL of heavy metal solution was added. The conical flask was placed in a shaker (WHY-2A, KEXI Instrument, China), and shaken for 180 min at a speed of 120 rpm. At regular intervals, the concentration of heavy metals in the solution before and after adsorption was measured by atomic absorption spectrometer (PinAAcle 900T, PerkinElmer, USA). In the multi-component solution, the initial concentration of heavy metal ions in each component was the same. Eqn (1) was used to calculate the adsorption capacity ($q_t$), and eqn (2) was used to calculate the removal efficiency ($\eta$). The experiment was repeated three times in parallel.

$$q_t\ (\text{mg g}^{-1}) = (C_0 - C_1) \times V/m \quad (1)$$

$$\eta\ (\%) = (C_0 - C_1)/C_0 \times 100 \quad (2)$$

where $C_0$ is the concentration of heavy metals in the solution before adsorption, mg $mL^{-1}$; $C_1$ is the concentration of heavy metals in the solution after adsorption, g $mL^{-1}$; $V$ is the volume of sample solution, mL; $m$ is the weight of sample, g.

### 2.5 Regenerative performance

After the adsorption experiment, MCA was removed from the solution and regenerated as follows. First, the free $Pb^{2+}$, $Cu^{2+}$ and $Cd^{2+}$ attached to the surface of MCA were removed by soaking in deionized water for 2 h. Then, MCA was eluted in 0.1 mol per L hydrochloric acid aqueous solution. Finally, it was repeatedly washed with deionized water to neutral, and then lyophilized. These processes were repeated five times, and the removal efficiency was used to evaluate this process.

## 3 Results and discussion

### 3.1 Characterization

The morphology and element distribution characteristics of MCA were characterized by SEM-EDS and TEM, and the results were shown in Fig. 1. The homogeneous bamboo pulp carbon-based aerogel (MCA1-1) shown in Fig. 1(a and b). After carbonization, MCA had rich 3D mesh pore structure. After further magnification (Fig. 1(b)), it was observed that the surface showed network structure, which provided more sites for $MnFe_2O_4$ particles. Fig. 1(c–e) showed the morphology of $MnFe_2O_4$ modified anisotropy bamboo pulp aerogel MCA1-3. Compared with the homogeneous MCA1-1, the cross section of MCA1-3 showed the same direction of the pore, while the longitudinal section showed the circular hole structure, indicating the anisotropy of the pore. Through further amplification and observation, spherical particles appeared on the surface of the smooth aerogel, which also confirmed the successful loading of $MnFe_2O_4$ particles.

In order to explore the effect of addition amount and carbonization temperature on the morphology of $MnFe_2O_4$ particles on the surface of the material more scientifically and intuitively, MCA1-1, MCA1-2, MCA1-3, MCA1-4, MCA2-1, MCA2-2 and MCA2-3 obtained by directional freezing are characterized by TEM, and the results were shown in Fig. 1(j–o). Fig. 1(j) (inset) showed that the surface of MCA1-1 without additives appeared particle-free, which were consistent with the SEM results. Fig. 1(j–l) showed that as the amount of additives increases, the point distribution of $MnFe_2O_4$ particles on the surface of the material tended to be obvious. Fig. 1(m–o) showed that when the carbonation temperature increased, the size of $MnFe_2O_4$ particles would increase significantly, and then the color of the particles in the picture would be deepened. In order to further explore the change of $MnFe_2O_4$ particle size,

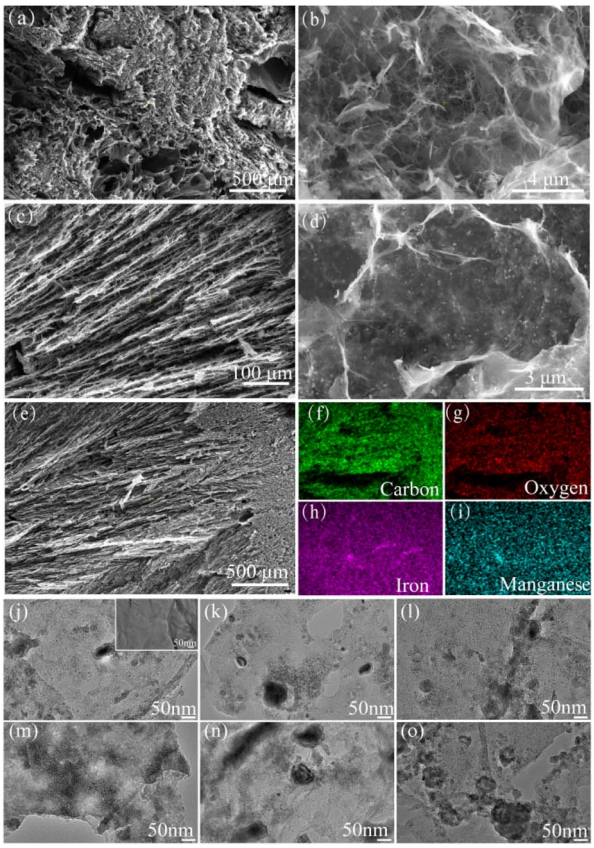


Fig. 1 (a and b) SEM images of MCA1-1 obtained by non directional freezing at different magnifications; (c–e) SEM images of MCA1-3 obtained by directional freezing at different magnifications; MCA1-3 element mapping ((f) carbon; (g) oxygen; (h) iron; (i) manganese); (j) MCA1-2 (inset: MCA1-1); (k) MCA1-3; (l) MCA1-4; (m) MCA2-1; (n) MCA2-2; (o) MCA2-3.

100 data points was collected in Fig. 1(j–o), and Origin 8.5 was used to analyze the relevant data and Gaussian fit, the results were shown in Fig. S1.† With the increase of additive dosage, the average diameter of the synthesized $MnFe_2O_4$ particles increased from 2.75 nm to 3.29 nm. When the carbonation temperature increased from 300 °C to 700 °C, the average diameter of $MnFe_2O_4$ particles increased from 2.25 nm to 3.64 nm.

The type of functional groups and pore structure have great influence on the adsorption performance of porous materials. In order to disclose the chemical and physical structure of MCA, the surface groups were characterized by XPS and XRD, and the pore structure was analyzed by BET. The obtained MCA1-1, MCA1-2, MCA1-3, and MCA2-3 after directional freezing were analyzed by XPS and XRD. The XPS full spectrum of MCA were shown in Fig. 2(a). The characteristic peaks of 284 eV, 552 eV, 642 eV and 711 eV represented C 1s, O 1s, Mn 2p and Fe 2p, respectively.[42] In addition, it was found that the peaks of Mn 2p (642 eV) and Fe 2p (711 eV) increased gradually with the increase of additives, while these two characteristic peaks (642 eV and 711 eV) were not found in the spectrogram of MCA1-1 without the addition of $MnFe_2O_4$, which also indicated that the successful loading of $MnFe_2O_4$ particles. It was consistent with the analysis of Fig. 1. The O 1s (552 eV) peak strengthened with the increase of the carbonation temperature, which was mainly caused by the increase of the precursor ablation efficiency after the temperature increased. In order to further explore the functional group structure of MCA, therefore, high-resolution XPS (C 1s, O 1s, Fe 2p, and Mn 2p) analysis of MCA1-3 was performed, and the results are shown in Fig. 2(b–e). Fig. 2(b) showed the fitting spectra of C 1s, which showed that there were three peaks associated with C–C (284.8 eV), C–O–C (286.3 eV), and O–C=O (288.6 eV) on the MCA surface,

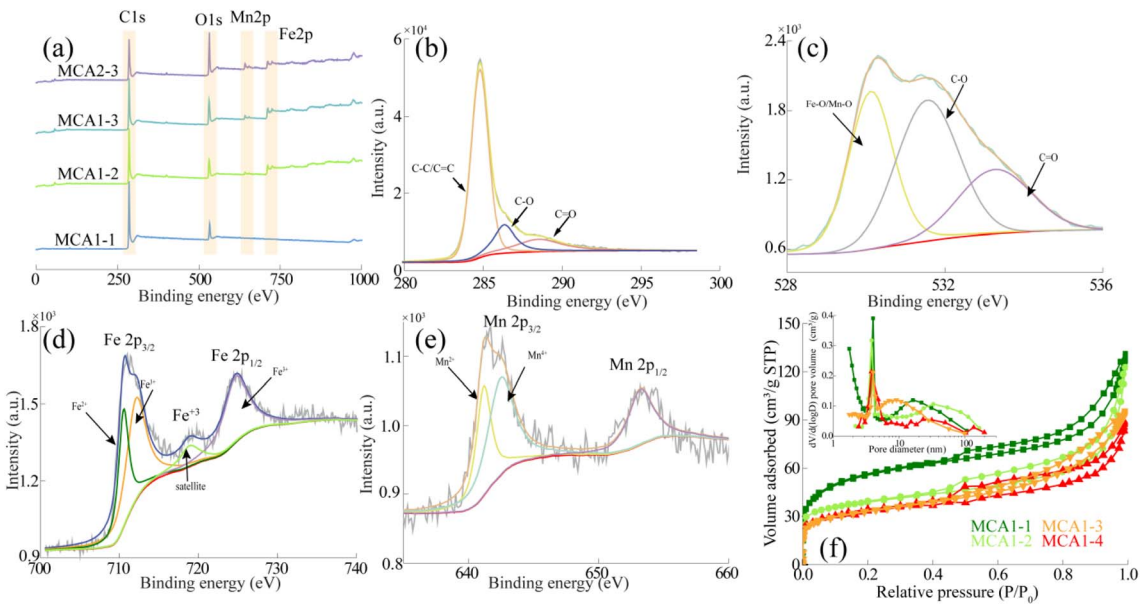


Fig. 2 (a) XPS spectrum of MCA; high-resolution XPS of MCA1-3: (b) C 1s, (c) O 1s, (d) Fe 2p; (e) Mn 2p; (f) $N_2$ adsorption–desorption isothermal curves of MCA, pore size distribution of MCA (inset).

indicating the presence of multiple C-containing functional groups. Fig. 2(c) showed the fitting spectra of O 1s, with three independent peaks at 530.1 eV, 531.6 eV and 532.82 eV, which represented Mn–O/Fe–O, C–O and C=O, respectively.[43] Fig. 2(d) showed the fitting spectra of Fe 2p, which had spin–orbit doublets of Fe $2p_{1/2}$ and Fe $2p_{3/2}$. The Fe $2p_{3/2}$ orbital could be divided into two peaks at binding energies of 711.0 eV and 712.3 eV, corresponding to the characteristic peaks of $Fe^{2+}$ and $Fe^{3+}$, respectively.[44] Fig. 2(e) showed the fitting spectra of Mn 2p, which had spin–orbit doublets of Mn $2p_{3/2}$ and Mn $2p_{1/2}$ with an orbital energy difference of 12 eV. The Mn $2p_{3/2}$ orbit had two peaks at 641.87 eV and 643.82 eV, corresponding to $Mn^{2+}$ and $Mn^{4+}$, respectively.[45] These results indicated that the MCA surface had a variety of functional groups (–C=O, –OH, Mn–O, and Fe–O), which played a key role in heavy metal adsorption. Fig. S2† showed the XRD results of MCA obtained from different preparation conditions. The diffraction peak of $2\theta$ at 21° showed a graphitic (002) plane, which indicated that MCA was composed of graphitic microcrystals. The diffraction peaks at 35.6, 44.8, 57.7 and 42.9 were represented (311), (400), (511) and (440) planes, indicating the presence of $MnFe_2O_4$ spinite ferrite structures on the MCA surface. These results were consistent with the previous XPS results.[46,47]

The amount of additive had a great influence on the pore structure of MCA. Therefore, in order to explore the effect of $MnFe_2O_4$ on the pore structure of MCA, the pore structure of MCA1-1, MCA1-2, MCA1-3 and MCA1-4 was analyzed by BET. The results were shown in Fig. 2(f), and the relevant data were shown in Table S1.† The $N_2$ adsorption–desorption isothermal curves of MCA loaded with $MnFe_2O_4$ or without $MnFe_2O_4$ being loaded showed the typical type IV curves.[48] In addition, the $N_2$ adsorption volume of MCA1-1, MCA1-2, MCA1-3, and MCA1-4 increased rapidly with increasing relative pressure at lower relative pressures, which indicated that the carbonization process caused more micropores in MCA. With the increase of $MnFe_2O_4$ loading, the adsorption volume of $N_2$ decreased, which indicated that $MnFe_2O_4$ occupied part of the micropores in MCA, resulting in the decrease of the specific surface area from 182.67 to 109.72 $m^2\ g^{-1}$. There were obvious hysteresis loops in the range of $P/P_0 = 0.40$–$1.00$, indicating the occurrence of capillary condensation, which indirectly proved the existence of mesoporous structures in MCA.

### 3.2 Adsorption studies of $Pb^{2+}$, $Cu^{2+}$ and $Cd^{2+}$

**3.2.1 Effects of preparation and adsorption conditions on adsorption performance of $Pb^{2+}$, $Cu^{2+}$ and $Cd^{2+}$.** In order to explore the effects of additive amount, freezing method, carbonization temperature, pH and initial concentration on $Pb^{2+}$, $Cu^{2+}$, $Cd^{2+}$ adsorption performance. MCA1-1, MCA1-2, MCA1-3, MCA1-4, MCA2-1, MCA2-2 and MCA2-3 prepared by directional and non-directional freezing, were selected for the adsorption evaluation, and the results were shown in Fig. 3. In general, the adsorption amount of MCA obtained by directional freezing was slightly higher than that obtained by non-directional freezing. With the increase of $MnFe_2O_4$ loading, the adsorption capacity of MCA prepared by directional freezing or non-directional freezing on $Pb^{2+}$, $Cu^{2+}$ and $Cd^{2+}$ showed a trend of first increasing and then decreasing. Due to the increase of $MnFe_2O_4$ loading, the adsorption sites increased. However, the excessive loading led to the formation of $MnFe_2O_4$ particle size was too large, the adsorption capacity began to decrease. Fig. 3(a–c) showed that when $MnFe_2O_4$ loading reached 20% and directional freezing was adopted, the adsorption capacities of MCA on $Pb^{2+}$, $Cu^{2+}$ and $Cd^{2+}$ all reached

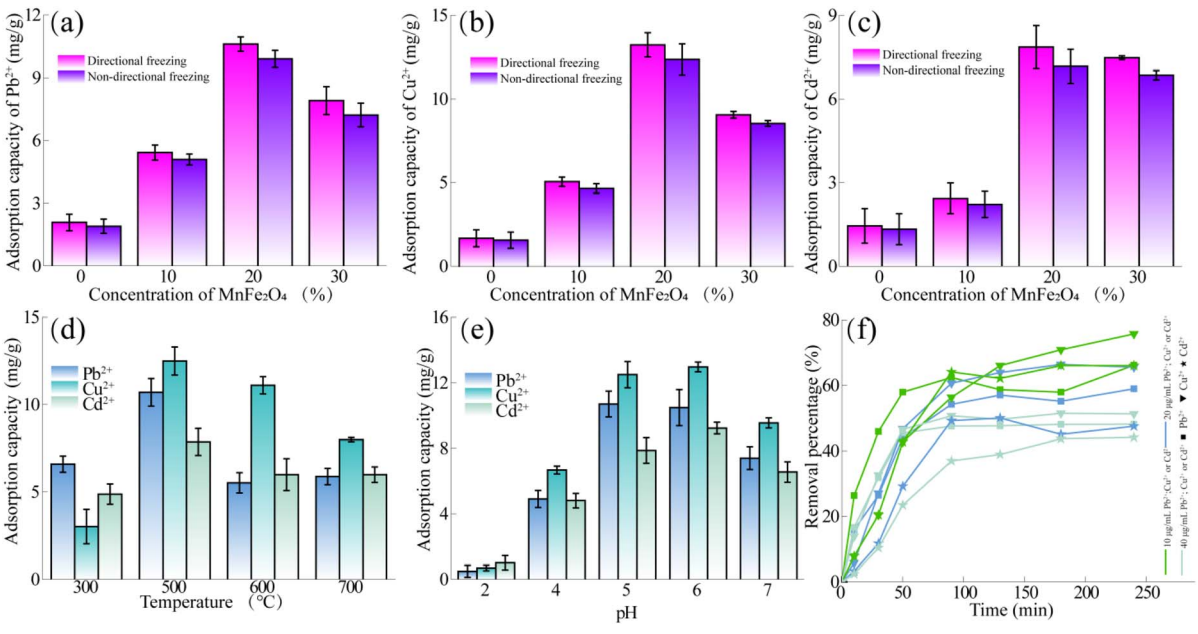


Fig. 3 Effects of MCA1-1, MCA1-2, MCA1-3 and MCA1-4 on adsorption capacity of (a) $Pb^{2+}$, (b) $Cu^{2+}$ and (c) $Cd^{2+}$; effect of (d) carbonation temperature, (e) pH and (f) initial concentration on the adsorption capacities of MCA1-3 towards $Pb^{2+}$, $Cu^{2+}$ and $Cd^{2+}$.

the maximum value, which were 10.60 mg $g^{-1}$, 13.23 mg $g^{-1}$ and 7.86 mg $g^{-1}$, respectively.

The carbonation temperature played a crucial role in the morphology and surface functional groups,[49] and then the adsorption effect could be affected. Therefore, the adsorption capacity of MCA2-1, MCA1-3, MCA2-2 and MCA2-3 for $Pb^{2+}$, $Cu^{2+}$ and $Cd^{2+}$ was investigated, and the results were shown in Fig. 3(d). With the increase of carbonization temperature, the adsorption capacity of $Pb^{2+}$, $Cu^{2+}$ and $Cd^{2+}$ by MCA firstly increased and then decreased. The reason for this phenomenon was that when the carbonization temperature was low (300 °C), the degree of MCA carbonization was incomplete. Meanwhile, the amount of $MnFe_2O_4$ generated by the loading was insufficient, resulting in the lower adsorption capacity. When the carbonization temperature reached 500 °C, the adsorption capacities of MCA on $Pb^{2+}$, $Cu^{2+}$ and $Cd^{2+}$ reached the maximum, and the adsorption capacities were 10.69 mg $g^{-1}$, 12.50 mg $g^{-1}$ and 7.86 mg $g^{-1}$, respectively. When the carbonization temperature was further increased (>500 °C), the carbonization degree of the matrix tended to stabilize. Nevertheless, according to the previous SEM results, it was found that high temperature caused the aggregation of the loaded $MnFe_2O_4$, the effective contact surface with heavy metals became decreasing, resulting in the decrease of adsorption capacity. In summary, considering the adsorption capacity of $Pb^{2+}$, $Cu^{2+}$ and $Cd^{2+}$ by anisotropy and isotropic MCA, MCA1-3 obtained by directional freezing was adopted as the main research object to conduct the following research work.

Fig. 3(e) showed that MCA had a significant impact on the adsorption capacity of $Pb^{2+}$, $Cu^{2+}$ and $Cd^{2+}$ at different pH, showing the trends of first increasing and then decreasing. Due to the binding of surface functional groups of MCA with $H^+$ at lower pH conditions, a repulsive force was formed between MCA and heavy metal ions, resulting in a decrease of adsorption capacity.[50] Therefore, the adsorption capacity of MCA for $Pb^{2+}$, $Cu^{2+}$ and $Cd^{2+}$ reached the maximum at pH = 6, which were 10.48 mg $g^{-1}$, 12.97 mg $g^{-1}$ and 9.23 mg $g^{-1}$, respectively. The results showed that the adsorption capacity of MCA for the three heavy metals was $Cu^{2+} > Pb^{2+} > Cd^{2+}$.

The initial heavy metal concentration is another important factor for the adsorption process. Therefore, the effects of initial heavy metal concentration on removal efficiency of anisotropic MCA successively with the concentration of $Pb^{2+}$, $Cu^{2+}$ and $Cd^{2+}$ of 10–40 μg $mL^{-1}$ were tested at the adsorption temperature of 25 °C, pH of 6, and the adsorption time of 240 min. The results were shown in Fig. 3(f). The removal efficiency of $Pb^{2+}$, $Cu^{2+}$ and $Cd^{2+}$ all showed a trend of increasing at first and then stabilizing with adsorption time. In addition, with the increase of initial concentrations, the removal efficiency decreased gradually. Due to some adsorption sites on the MCA surface were incompletely occupied at low initial concentrations, so the removal efficiency was high. When the initial concentration was high, there was no excess adsorption sites on the MCA surface to adsorb heavy metals, so the removal efficiency gradually decreases.[51]

**3.2.2 Adsorption kinetics and isotherms.** In order to elucidate the adsorption rate control steps and absorption types, the adsorption kinetic data were fitted with pseudo-first-order and pseudo-second-order kinetic models, following formulae eqn (S1) and (S2).† Fig. 4 showed the kinetics studies of single, binary, and ternary systems of $Pb^{2+}$, $Cu^{2+}$, and $Cd^{2+}$ at different concentrations (20–60 μg $mL^{-1}$) by

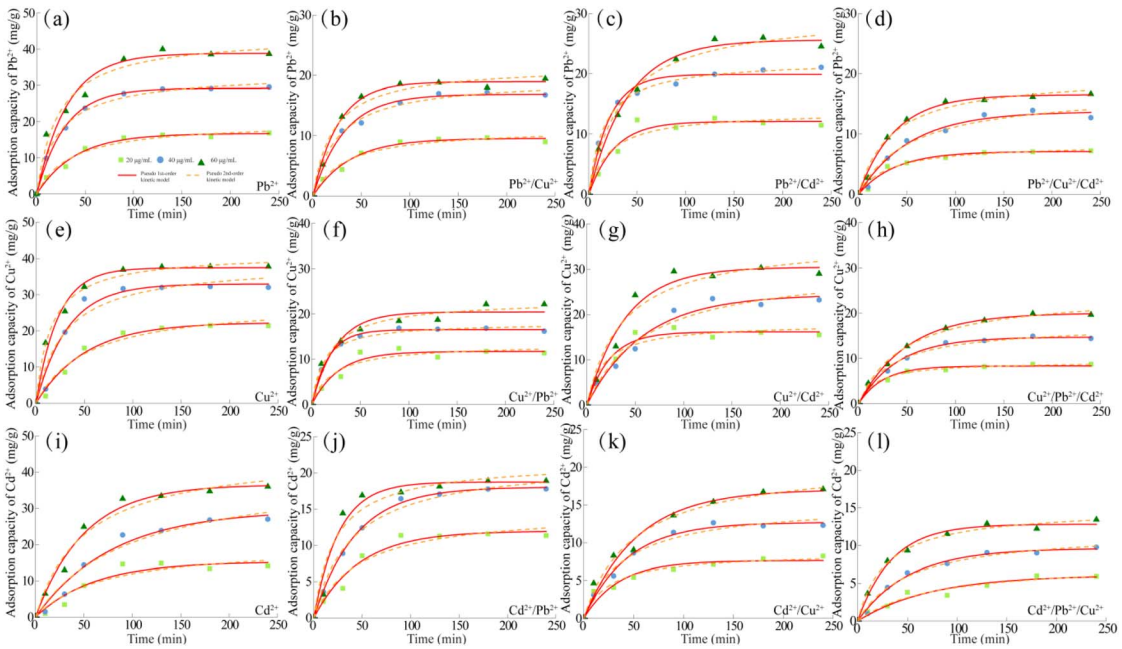


Fig. 4 Pseudo-first-order and pseudo-second-order models for $Pb^{2+}$ in the system of: (a) $Pb^{2+}$, (b) $Pb^{2+}/Cu^{2+}$, (c) $Pb^{2+}/Cd^{2+}$, (d) $Pb^{2+}/Cu^{2+}/Cd^{2+}$; $Cu^{2+}$ in the system of: (e) $Cu^{2+}$, (f) $Cu^{2+}/Pb^{2+}$, (g) $Cu^{2+}/Cd^{2+}$, (h) $Cu^{2+}/Pb^{2+}/Cd^{2+}$; $Cd^{2+}$ in the system of: (i) $Cd^{2+}$, (j) $Cd^{2+}/Pb^{2+}$, (k) $Cd^{2+}/Cu^{2+}$, (l) $Cd^{2+}/Pb^{2+}/Cu^{2+}$ on the MCA, at pH = 6 and temperature = 25 °C.

MCA. The results showed that with the extension of adsorption time, the adsorption capacity increased rapidly from the beginning and gradually became stable. With the increase of time, the adsorption sites of MCA was occupied, and then the adsorption rate gradually decreased. Meanwhile, the adsorption of $Pb^{2+}$, $Cu^{2+}$ and $Cd^{2+}$ by MCA increased gradually with the increase of heavy metal concentration. This phenomenon was mainly explained by the fact that the high concentration of heavy metals would strengthen transferring of heavy metal to the surface of MCA and finally provide a greater possibility for MCA adsorption. In addition, the adsorption capacity of $Pb^{2+}$, $Cu^{2+}$ and $Cd^{2+}$ by MCA in the solution of single system was higher than that of binary and ternary systems, which was mainly because heavy metals competed with each other for the adsorption sites on the surface of MCA in the multi-system system. The correlation coefficient in the adsorption process were fitted, and the results were shown in Tables S2–S4.† The pseudo-first-order kinetic model was better fitted than the pseudo-second-order kinetic model for most adsorption processes. The adsorption process involved not only physical adsorption process, but also chemical adsorption process.

In order to accurately describe the adsorption mechanism of MCA on $Pb^{2+}$, $Cu^{2+}$ and $Cd^{2+}$ at a certain temperature, Langmuir adsorption isothermal model and Freundlich adsorption isothermal model were used to fit the relevant data, following formulae eqn (S3) and (S4).† Fig. 5 showed the adsorption isothermal curves of MCA for $Pb^{2+}$, $Cu^{2+}$ and $Cd^{2+}$ in the single, binary and ternary systems discussed at different temperatures. At the same time, the adsorption capacity of MCA for $Pb^{2+}$, $Cu^{2+}$ and $Cd^{2+}$ increased with the increase of temperature, indicating that the adsorption process was endothermic and the increase of temperature was conducive to the adsorption. Relevant data were fitted and the adsorption isothermal curve parameters were shown in Tables S5–S7.† The results showed that most of the adsorption isothermal curves of MCA for $Pb^{2+}$, $Cu^{2+}$ and $Cd^{2+}$ could be described by Langmuir isothermal curves, indicating that the process was involved in chemisorption. Finally, when the temperature was at 45 °C, the maximum adsorption capacity of MCA for $Pb^{2+}$ in the systems of $Pb^{2+}$, $Pb^{2+}/Cu^{2+}$, $Pb^{2+}/Cd^{2+}$ and $Pb^{2+}/Cu^{2+}/Cd^{2+}$ were 74.38 mg $g^{-1}$, 37.01 mg $g^{-1}$, 55.26 mg $g^{-1}$ and 37.49 mg $g^{-1}$, respectively. The maximum adsorption capacities for $Cu^{2+}$ in the systems of $Cu^{2+}$, $Cu^{2+}/Pb^{2+}$, $Cu^{2+}/Cd^{2+}$ and $Cu^{2+}/Pb^{2+}/Cd^{2+}$ were 84.21 mg $g^{-1}$, 67.07 mg $g^{-1}$, 52.63 mg $g^{-1}$ and 36.14 mg $g^{-1}$, respectively. The maximum adsorption capacity for $Cd^{2+}$ in the systems of $Cd^{2+}$, $Cd^{2+}/Pb^{2+}$, $Cd^{2+}/Cu^{2+}$ and $Cd^{2+}/Pb^{2+}/Cu^{2+}$ systems were 73.63, 26.47, 55.35 and 36.29 mg $g^{-1}$, respectively.

In order to clearly understand the energy change in the adsorption process, eqn (S5)–(S8) were used to calculate the thermodynamic parameters of the adsorption process, and the results are shown in Tables S8–S10.† In single, binary and ternary systems, the adsorption thermodynamic parameter of MCA to $Pb^{2+}$, $Cu^{2+}$ and $Cd^{2+}$, $\Delta G^{\theta}$ was negative, indicating that the adsorption processes were spontaneous. $\Delta H^{\theta} > 0$ reflected the endothermic nature of the adsorption process. $\Delta S^{\theta} > 0$ indicated an increase in degrees of freedom at the solid–liquid interface during adsorption. It showed that the increase of temperature in the adsorption process was beneficial to the adsorption.[52]

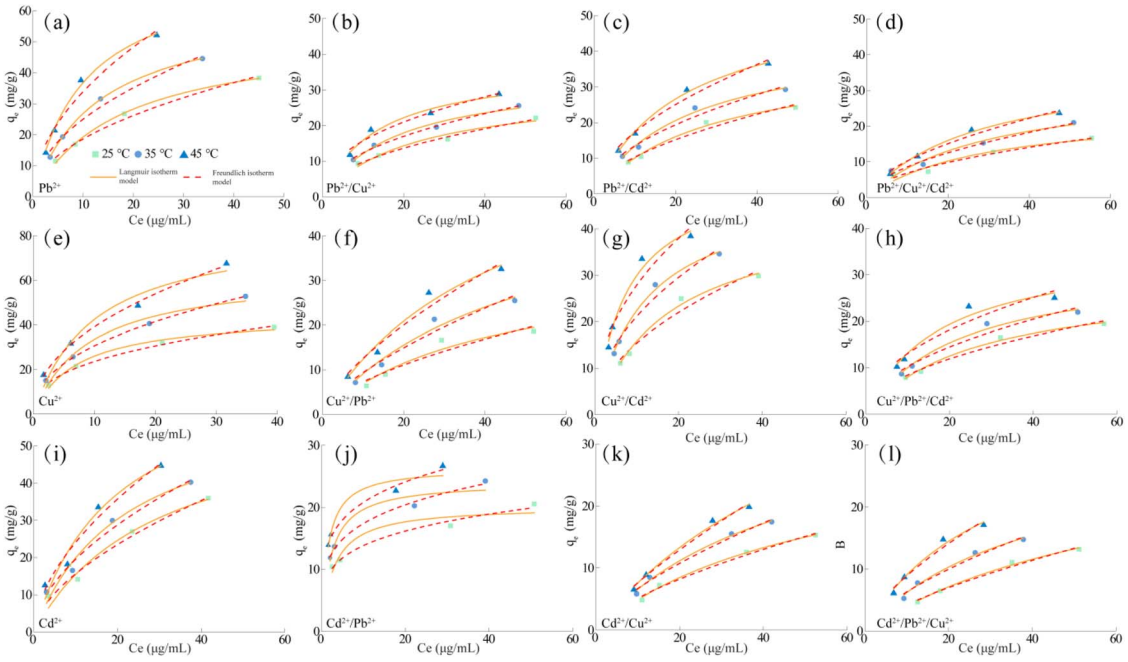


Fig. 5 Langmuir and Freundlich adsorption isothermal curves for $Pb^{2+}$ in the system of: (a) $Pb^{2+}$, (b) $Pb^{2+}/Cu^{2+}$, (c) $Pb^{2+}/Cd^{2+}$, (d) $Pb^{2+}/Cu^{2+}/Cd^{2+}$; $Cu^{2+}$ in the system of: (e) $Cu^{2+}$, (f) $Cu^{2+}/Pb^{2+}$, (g) $Cu^{2+}/Cd^{2+}$, (h) $Cu^{2+}/Pb^{2+}/Cd^{2+}$; $Cd^{2+}$ in the system of: (i) $Cd^{2+}$, (j) $Cd^{2+}/Pb^{2+}$, (k) $Cd^{2+}/Cu^{2+}$, (l) $Cd^{2+}/Pb^{2+}/Cu^{2+}$ on the MCA.

Table 1 Adsorption distribution coefficient and selectivity factor of MCA for $Pb^{2+}$, $Cu^{2+}$ and $Cd^{2+}$ in single, binary and ternary systems[a]

| Adsorbate | $K_{dA}$ | $K_{dM}$ | $\alpha_M^A$ |
|---|---|---|---|
| $Pb^{2+}$ | 2.0039 | — | — |
| $Cu^{2+}$ | 3.0623 | — | — |
| $Cd^{2+}$ | 1.3424 | — | — |
| $Pb^{2+}/Cu^{2+}$ | 0.5792 | 0.9110 | 0.6358 |
| $Pb^{2+}/Cd^{2+}$ | 0.9620 | 0.9375 | 1.0262 |
| $Cu^{2+}/Cd^{2+}$ | 1.3873 | 0.4755 | 2.9176 |
| $Pb^{2+}/Cu^{2+}/Cd^{2+}$ | 0.4780 | 0.9305 | 1.0478 |
| $Cu^{2+}/Pb^{2+}/Cd^{2+}$ | 0.5723 | 0.8362 | 1.3863 |
| $Cd^{2+}/Pb^{2+}/Cu^{2+}$ | 0.3582 | 1.0503 | 0.6820 |

[a] The first metal ion represents the target ion A, the other ions represent the interfering ion M.

### 3.3 Adsorption selectivity

In order to explore the selective adsorption of MCA to $Pb^{2+}$, $Cu^{2+}$ and $Cd^{2+}$ in the binary, and ternary systems, 20 μg per mL heavy metals concentration were selected for evaluation by the distribution coefficient ($K_d$) and adsorption $\alpha_M^A$ selectivity factor. The calculation formulae were shown in eqn (S7) and (S8),† respectively.

Table 1 showed the adsorption distribution coefficients and selectivity factors of $Pb^{2+}$, $Cu^{2+}$ and $Cd^{2+}$ by MCA in single, binary and ternary systems. The results showed that MCA adsorbed $Cu^{2+}$ preferently, followed by $Pb^{2+}$ and $Cd^{2+}$. At the same time, it was found that there was a competitive adsorption among $Pb^{2+}$, $Cu^{2+}$ and $Cd^{2+}$ during the adsorption process of MCA. A similar result could be obtained by studying the selectivity factor.

### 3.4 Adsorption mechanism

In order to explore the functional group changes on the surface of MCA, FTIR analysis was performed on MCA1-1 and MCA1-3 before and after adsorption, and the results were shown in Fig. 6. According to the MCA1-1 FTIR results, the peaks of 3420 $cm^{-1}$, 1620 $cm^{-1}$ and 1040 $cm^{-1}$ represented the stretching vibration of O–H, the stretching vibration of C=O and the bending vibration of C–O, respectively. Compared with the MCA1-1, MCA1-3 loaded with $MnFe_2O_4$ showed a new peak at 523 $cm^{-1}$, and 1440 $cm^{-1}$, which were mainly caused by Fe–O/Mn–O and the bending vibration of O–H. Moreover, when MCA1-3 adsorbed $Pb^{2+}$, $Cu^{2+}$ and $Cd^{2+}$, the peak of 523 $cm^{-1}$ became smaller and the wave number moved to 605 $cm^{-1}$. At the same time, the peak of 3420 $cm^{-1}$ moved to 3410 $cm^{-1}$ and the peak of 1440 $cm^{-1}$ disappeared, indicating that a large amount of hydroxyl groups had ion exchange with the heavy metals. In conclusion, the surface functional groups of MCA1-1 were mainly oxygen-containing groups such as hydroxyl, carbonyl and carboxyl. When loaded with $MnFe_2O_4$, additional surface functional groups were added including Fe–O, Mn–O, *etc.* The results were similar to those results for the adsorption process of magnetic $MnFe_2O_4$–biochar composites by Zhang *et al.*[53] Therefore, the adsorption reaction of MCA surface functional groups on heavy metal ions $M^{2+}$ ($M^{2+}$ = $Pb^{2+}$, $Cu^{2+}$, $Cd^{2+}$) involved the following eqn (i)–(iv):

$$(Mn)Fe\text{–}OH + M^{2+} \rightarrow (Mn)Fe\text{–}O^{-}\text{–}M^{2+} + H^{+}; \quad \text{(i)}$$

$$((Mn)Fe\text{–}OH)_2 + M^{2+} \rightarrow ((Mn)Fe\text{–}O\text{–})_2\text{–}M^{2+} + 2H^{+}; \quad \text{(ii)}$$

$$\text{–}COOH + M^{2+} \rightarrow \text{–}COO^{-}\text{–}M^{2+} + H^{+}; \quad \text{(iii)}$$

$$(\text{–}COOH)_2 + M^{2+} \rightarrow (\text{–}COO\text{–})_2\text{–}M^{2+} + 2H^{+}; \quad \text{(iv)}$$

Zeta potential was an important parameter to evaluate the nature of the surface charge of adsorbent particles, while the pH zero point of charge ($pH_{zpc}$) represented the electrophoretic mobility when the net total particle charge was zero.[54] The zeta potential of MCA1-3 at room temperature was studied under different pH conditions, as shown in Fig. S3.† It could be

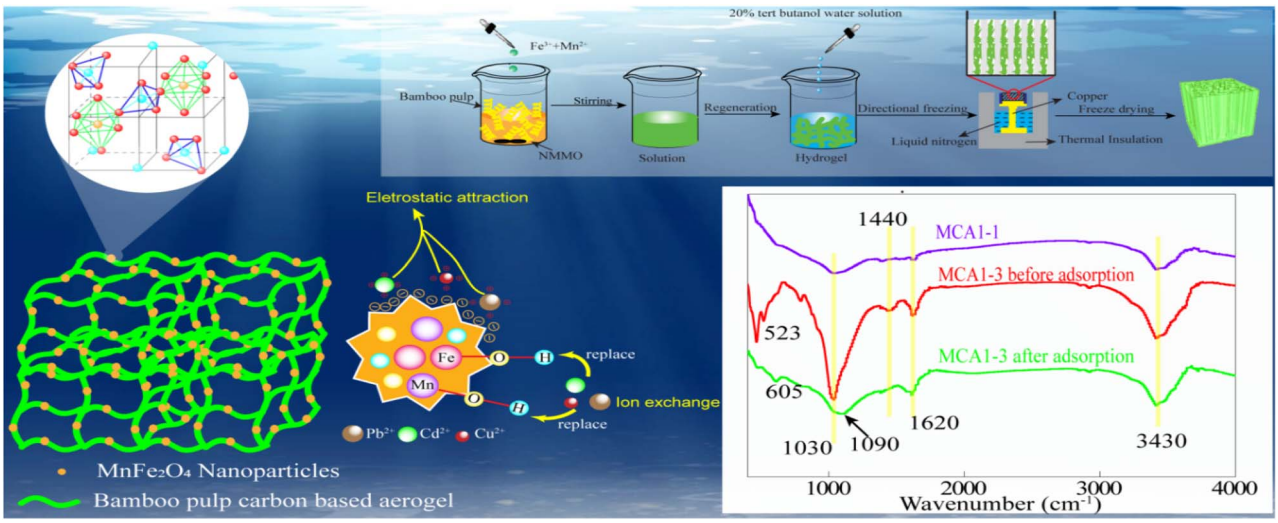


Fig. 6 FTIR of before and after adsorption and possible mechanism of the adsorption of MCA on $Pb^{2+}$, $Cu^{2+}$ and $Cd^{2+}$.

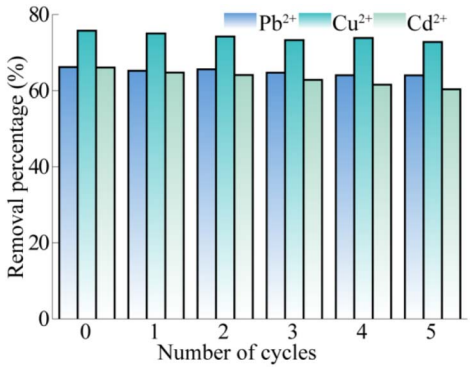


Fig. 7 Removal efficiency of $Pb^{2+}$, $Cu^{2+}$ and $Cd^{2+}$ by MCA in 5 adsorption–desorption cycles.

confirmed that the surface charge of MCA was positive at pH < 4.89, leading to a repulsion between the MCA and the heavy metals. However, when pH > 4.89, the surface charge of MCA became negative. The negative charge on the surface favored the adsorption of heavy metals by electrostatic interactions.

### 3.5 Desorption and regeneration

The regeneration of adsorbent was an important index to determine the cost and stability of materials. The MCA after adsorption was repeatedly immersed in 0.1 mol per L hydrochloric acid to desorb $Pb^{2+}$, $Cu^{2+}$ and $Cd^{2+}$. Then, the desorbed MCA was washed repeatedly using deionized water until the washed water was nearly neutral. At low pH, there is a fairly high concentration of hydrogen ions around the binding site of the adsorbent, which competes strongly with the positively charged heavy metal ions, resulting in strong electrostatic repulsion of metal cations and a longer distance between the adsorbent and adsorbate.[55,56] After 5 cycles (the results are shown in the Fig. 7), the removal efficiency of $Pb^{2+}$, $Cu^{2+}$ and $Cd^{2+}$ were 63.97%, 72.73% and 60.29%, respectively, which were slightly lower than those at the beginning (decreased by 3.32%, 3.96% and 8.69%, respectively). Therefore, MCA was a good candidate material for adsorption in future, due to its remarkable regenerative and recyclability. For comparison, we retrieved the metal ion adsorption capacity of other biomass carbon-based adsorbents, and systematically listed adsorbents, adsorbates and the adsorption capacity. As shown in Table S11,† in our work, MCA was used as a capture agent for adsorption of heavy metals $Pb^{2+}$, $Cu^{2+}$, $Cd^{2+}$ with the maximum adsorption capacities of 74.38, 84.21 and 73.63 mg $g^{-1}$, respectively, which was better than the related research progress.[57–60] It has a certain application prospect in water pollution control.

## 4 Conclusions

In this paper, $MnFe_2O_4$-modified bamboo pulp carbon-based aerogel (MCA) was prepared by *in situ* loading $MnFe_2O_4$, freeze-drying and carbonization. MCA had a 3D network structure, and the pores were anisotropy with high porosity (80.88%) and large specific surface area (>100 $m^2$ $g^{-1}$). Because of its magnetic properties, it was easy to recycle after use. The surface had a variety of functional groups such as –C=O, –OH, Mn–O, and Fe–O, which played a key role in heavy metal adsorption. Through the study of adsorption kinetics, adsorption isothermal curve and adsorption thermodynamic parameters, it was found that MCA had a heterogeneous surface and the adsorption process involved not only physical adsorption, but also chemical adsorption in the single, binary and ternary systems, and the adsorption process was also a spontaneous endothermic process. The maximum adsorption capacities of MCA for $Pb^{2+}$, $Cu^{2+}$ and $Cd^{2+}$ were 74.38, 84.21 and 73.63 mg $g^{-1}$, respectively. The removal ability of MCA for $Pb^{2+}$, $Cu^{2+}$ and $Cd^{2+}$ in the multi-system adsorption process was as follows: $Cu^{2+}$ > $Pb^{2+}$ > $Cd^{2+}$, and there was competitive adsorption among heavy metals during the adsorption process. Therefore, MCA had potential applications in the purification of heavy metal wastewater containing $Pb^{2+}$, $Cu^{2+}$ and $Cd^{2+}$. The results provided basic scientific basis and theoretical reference for the development of environmental functional materials with high efficiency in removing heavy metals from water using bamboo pulp as raw material.

## Data availability

The data supporting this article have been included as part of the ESI.†

## Author contributions

Wenxiang Jing: methodology, writing – review & editing. Chai Yang: data curation, resources. Xiaoyan Lin: conceptualization, supervision. Min Tang: resources. Dongming Lian: funding acquisition. Ying Yu: project administration. Dongyang Liu: resources.

## Conflicts of interest

There are no conflicts to declare.

## Acknowledgements

The authors would like to thank the financials support from Longshan Academic Talent research support plan of Southwest University of Science and Technology (18lzx315), Sichuan Science and Technology Program (2019YFN0029). This work was also sponsored by the project commissioned by Zhejiang Junkang Technology Co., Ltd (20zh0203).

## References

1 G. A. Engwa, P. U. Ferdinand, F. N. Nwalo and M. N. Unachukwu, *Poisoning in the Modern World-New Tricks for an Old Dog*, 2019, vol. 10, pp. 70–90.
2 Q. Zhou, N. Yang, Y. Li, B. Ren, X. Ding, H. Bian and X. Yao, *Glob. Ecol. Conserv.*, 2020, **22**, e00925.
3 L. Hai, M. Zhou, B. Li and Y. Dong, *Int. Biodeterior. Biodegrad.*, 2023, **178**, 105544.

4 X. Yang, L. Liu, Y. Wang, T. Lu, Z. Wang and G. Qiu, *Environ. Pollut.*, 2023, **320**, 121002.
5 J. Kim, H. Kim and K. Baek, *Sci. Total Environ.*, 2023, **886**, 163891.
6 S. A. Gouda and A. Taha, *Egypt. J. Aquat. Biol. Fish.*, 2023, **27**, 135–153.
7 J. T. Mathew, C. O. Adetunji, A. Inobeme, M. Monday, Y. Azeh, A. A. Otori, E. Y. Shaba, A. Mamman and T. Ezekiel, *Modern Approaches in Waste Bioremediation*, 2023, pp. 117–130.
8 P. K. Chaurasia, N. Nagraj, N. Sharma, S. Kumari, M. Yadav, S. Singh, A. h. Mani, S. Yadava and S. L. Bharati, *Biotechnol. Bioeng.*, 2023, **120**, 57–81.
9 K. Wang, F. Zhang, K. Xu, Y. Che, M. Qi and C. Song, *RSC Adv.*, 2023, **13**, 6713–6736.
10 B. Wang, J. Lan, C. Bo, B. Gong and J. Ou, *RSC Adv.*, 2023, **13**, 4275–4302.
11 N. A. A. Qasem, R. H. Mohammed and D. U. Lawal, *npj Clean Water*, 2021, **4**, 36.
12 Z. Feng, P. Wang, Y. Cheng, Y. Mo, X. Luo, P. Liu, R. Guo and X. Liu, *J. Electroanal. Chem.*, 2023, **946**, 117703.
13 M. Ghobadi, M. Gharabaghi, H. Abdollahi, Z. Boroumand and M. Moradian, *J. Hazard. Mater.*, 2018, **351**, 308–316.
14 L. A. Melinia, M. Naibaho, E. Puspita, R. Ramlan and M. Ginting, *Indonesian Physical Review*, 2023, **6**, 196–219.
15 C. R. Kalaiselvan, S. S. Laha, S. B. Somvanshi, T. A. Tabish, N. D. Thorat and N. K. Sahu, *Coord. Chem. Rev.*, 2022, **473**, 214809.
16 K. Malaie and M. R. Ganjali, *J. Energy Storage*, 2021, **33**, 102097.
17 Z. Ma, D. Zhao, Y. Chang, S. Xing, Y. Wu and Y. Gao, *Dalton Trans.*, 2013, **42**, 14261.
18 M. S. Podder and C. B. Majumder, *J. Mol. Liq.*, 2015, **212**, 382.
19 N. Akhlaghi and G. Najafpour-Darzi, *J. Ind. Eng. Chem.*, 2021, **103**, 292–304.
20 S. J. Salih and W. M. Mahmood, *Heliyon*, 2023, **9**, e16601.
21 S. S. Sonu, V. Dutta, P. Raizada, A. Hosseini-Bandegharaei, V. Thakur, V. Nguyen, Q. VanLe and P. Singh, *J. Environ. Chem. Eng.*, 2021, **9**, 105812.
22 A. Asha, K. C. Juglan and A. Jain, *AIP Conf. Proc.*, 2024, 29–30.
23 Y. Zohrabi, *Mater. Sci. Eng. B*, 2024, **299**, 117024.
24 M. O. Nwodo, R. M. Obodo, A. C. Nwanya, A. B. C. Ekwealor and F. I. Ezema, *Electrode Materials for Energy Storage and Conversion*, 2021, vol. 1, p. 42.
25 M. E. C. Ferreira, E. G. Bernardino, M. A. S. D. de Barros, R. Bergamasco and N. U. Yamaguchi, *J. Water Proc. Engineering*, 2023, **54**, 104049.
26 N. Chaibakhsh and Z. Moradi-Shoeili, *Mater. Sci. Eng. C*, 2019, **99**, 1424–1447.
27 H. Li, H. Ji, X. Cui, X. Che, Q. Zhang, J. Zhong, R. Jin, L. Wang and Y. Luo, *Int. J. Min. Sci. Technol.*, 2021, **31**, 1107–1115.
28 J. Li, M. Zhang, Q. Kong, T. Zeng, Y. Mao, J. Liu and S. Xie, *J. Taiwan Inst. Chem. Eng.*, 2024, **166**, 105532.
29 M. Verma, A. Kumar, K. P. Singh, R. Kumar, V. Kumar, C. M. Srivastava, V. Rawat, G. Rao, S. Kumari, P. Sharma and H. Kim, *J. Mol. Liq.*, 2020, **315**, 113769.
30 R. Asadi, H. Abdollahi, M. Gharabaghi and Z. Boroumand, *Adv. Powder Technol.*, 2020, **31**, 1480.
31 F. Güzel and C. Yılmaz, *J. Environ. Chem. Eng.*, 2021, **9**, 104567.
32 J. Liu, S. Ren, J. Cao, D. C. W. Tsang, J. Beiyuan, Y. Peng, F. Fang, J. She, M. Yin, N. Shen and J. Wang, *J. Hazard. Mater.*, 2021, **401**, 123311.
33 C. Chen, H. Li, A. Dauletbek, F. Shen, D. Hui, M. Gaff and R. Lorenzo, *J. Renewable Mater.*, 2022, **10**, 605–624.
34 F. Rusch, A. D. Wastowski, T. S. de Lira, K. C. C. S. R. Moreira and D. de M. Lúcio, *Biomass Convers. Biorefin.*, 2023, **13**, 2487–2495.
35 M. F. Esa, N. M. Main, M. N. Roslan, N. Marsi, K. Kamarudin and L. Jasmani, *Technological Advancement in Instrumentation & Human Engineering*, 2023, vol. 882, pp. 363–385.
36 L. Chen, X. Jiang, N. Qu, H. Lu, J. Xu, Y. Zhang and G. Li, *Mater. Today Sustain.*, 2022, **19**, 10028.
37 M. M. Rashid, N. Abir, M. A. Hossain, M. I. Iqbal and A. B. Siddique, *Cellulose Fibre Reinforced Composites*, 2023, pp. 23–48.
38 Q. Lin, Y. Huang and W. Yu, *Carbohydr. Polym.*, 2020, **241**, 116412.
39 V. K. G. Suhas, P. J. M. Carrott, R. Singh, M. Chaudhary and S. Kushwaha, *Bioresour. Technol.*, 2016, **216**, 1066.
40 J. Lamaming, S. Saalah, M. Rajin, N. M. Ismail and A. Z. Yaser, *Int. J. Chem. Eng.*, 2022, **2022**, 14.
41 X. Hou, J. Feng, Y. Ren, Z. Fan and M. Zhang, *Colloids Surf., A*, 2010, **363**, 1–7.
42 W. Xu, Y. Song, K. Dai, S. Sun, G. Liu and J. Yao, *J. Hazard. Mater.*, 2018, **358**, 337–345.
43 Y. Shen, F. Fu and B. Tang, *J. Environ. Chem. Eng.*, 2023, **11**, 110230.
44 Z. Liu, G. Chen, F. Hu and X. Li, *J. Environ. Manage.*, 2020, **263**, 110377.
45 Y. Chen, F. Xu, H. Li, Y. Li, Y. Liu, Y. Chen, M. Li, L. Li, H. Jiang and L. Chen, *J. Anal. Appl. Pyrolysis*, 2021, **156**, 105173.
46 Z. Ma, D. Zhao, Y. Chang, S. Xing, Y. Wua and Y. Gao, *Dalton Trans.*, 2013, **42**, 14261–14267.
47 F. Güzel and C. Yılmaz, *J. Environ. Chem. Eng.*, 2021, **9**, 104567.
48 F. B. Loulic, R. H. S. M. Shirazi, M. Miralinaghi, H. A. Panahi and E. Moniri, *Microporous Mesoporous Mater.*, 2023, **356**, 112567.
49 O. E. Cigarroa-Mayorga, *Ceram. Int.*, 2021, **47**, 32397–32406.
50 R. Asadi, H. Abdollahi, M. Gharabaghi and Z. Boroumand, *Adv. Powder Technol.*, 2020, **31**, 1480–1489.
51 T. Suwunwong, P. Danwittayakul, C. Thanomsilp, P. Siriwat, S. Chantrapromma and K. Phoungthong, *Mater. Res. Express*, 2021, **8**, 015505.
52 W. Jing, L. Yin, X. Lin, Y. Yu, D. Lian, Z. Shi, P. Chen, M. Tang and C. Yang, *Polymers*, 2022, **14**, 4909.
53 L. Zhang, J. Guo, X. Huang, W. Wang, P. Sun, Y. Li and J. Han, *RSC Adv.*, 2019, **9**, 365–376.
54 L. Cui, Y. Wang, L. Gao, L. Hu, L. Yan, Q. Wei and B. Du, *Chem. Eng. J.*, 2015, **281**, 1.

55 T. Liu, S. Gou, Y. He, S. Fang, L. Zhou, G. Gou and L. Liu, *Carbohydr. Polym.*, 2021, **269**, 118355.
56 I. Ihsanullah, M. Sajid, S. Khan and M. Bilal, *Sep. Purif. Technol.*, 2022, **291**, 120923.
57 H. Asadollahzadeh, M. Ghazizadeh and M. Manzari, *Anal. Methods Environ. Chem. J.*, 2021, **4**, 33.
58 M. Zahedifar, N. Seyedi, S. Shafiei and M. Basij, *Mater. Chem. Phys.*, 2021, **217**, 12460.
59 S. Cairns, S. Chaudhuri, G. Sigmund, I. Robertson, N. Hawkins, T. Dunlop and T. Hofmann, *Environ. Technol. Innovation*, 2021, **24**, 101961.
60 L. Mészáros, M. Šuránek, Z. Melichová, V. Frišták, L. Ďuriška, M. Kaňuchová, G. Soja and M. Pipíškal, *J. Radioanal. Nucl. Chem.*, 2023, **332**, 4141.